ISSN: 1672 - 6553

JOURNAL OF DYNAMICS AND CONTROL

VOLUME 9 ISSUE 12: P52-80

COMPUTATIONAL STUDY ON CONVECTION AND RADIATIVE HEAT TRANSFER IN COPPER-WATER NANOFLUIDS FOR THERMAL ENGINEERING APPLICATIONS

Y. Veeranna[1], C. P. Pooja[3], B. S. Prathibha[2], P. B. Sampath Kumar[3,4]

[1]*Department of Studies and Research in Mathematics, Government Science College (Autonomous), Bengaluru-560001, Karnataka, India.*

[2]*Government Sri Krishnarajendra Silver Jubilee Technological Institute, Bangalore-560001, Karnataka, India.*

[3]*Department of Mathematics, PG Centre Ramanagara, Bangalore University, Ramanagara-562159, Karnataka, India.*

[4]*Universidad Bernardo O'Higgins, Facultad de Ingeniería, Ciencia y Tecnología, Departamento de Formación y Desarrollo Científico en Ingeniería, Av. Viel 1497, Santiago, Chile.*

JOURNAL OF DYNAMICS AND CONTROL
https://doi.org/10.71058/jodac.v9i12004

COMPUTATIONAL STUDY ON CONVECTION AND RADIATIVE HEAT TRANSFER IN COPPER-WATER NANOFLUIDS FOR THERMAL ENGINEERING APPLICATIONS

Y. Veeranna[1@], C. P. Pooja[3$], B. S. Prathibha[2#], P. B. Sampath Kumar[3,4*]

[1]*Department of Studies and Research in Mathematics, Government Science College (Autonomous), Bengaluru-560001, Karnataka, India.*

[2]*Government Sri Krishnarajendra Silver Jubilee Technological Institute, Bangalore-560001, Karnataka, India.*

[3]*Department of Mathematics, PG Centre Ramanagara, Bangalore University, Ramanagara-562159, Karnataka, India.*

[4]*Universidad Bernardo O'Higgins, Facultad de Ingeniería, Ciencia y Tecnología, Departamento de Formación y Desarrollo Científico en Ingeniería, Av. Viel 1497, Santiago, Chile.*

[@]*veerannahariyabbe@gmail.com,* [$]*poojacp740@gmail.com,* [#]*prathi.chikkaiah@gmail.com,*
[*]*sampathkumarpb123@gmail.com*

[*]***Corresponding author***

Abstract: This paper presents a numerical analysis of three-dimensional convection flow and heat transfer in a copper–water nanofluid, incorporating key thermal effects relevant to modern engineering applications. The model accounts for thermal radiation, viscous dissipation, Joule heating, and spatially dependent internal heat generation. Similarity transformations reduce the governing equations to a system of nonlinear ordinary differential equations, solved using the Runge-Kutta-Fehlberg (RKF) method. Results show that electromagnetic forces combined with localized heat sources significantly elevate temperature distribution and thermal boundary layer thickness. The copper–water nanofluid exhibits superior heat transfer performance due to its high thermal conductivity.

Keywords: Copper–water nanofluid; Mixed convection; Thermal radiation; Viscous dissipation; Joule heating; Slip flow; Exponential heat source.

https://doi.org/10.71058/jodac.v9i12004

1. Introduction

In many practical thermal systems, the transport of heat within a fluid occurs due to a combination of two fundamental mechanisms: forced convection, driven by external influences such as a moving surface or pump-induced flow, and natural (free) convection, which arises from buoyancy forces due to temperature gradients within the fluid. When these two mechanisms act simultaneously, the phenomenon is referred to as mixed convection. Mixed convection plays a crucial role in a wide variety of engineering applications, including heat exchangers, electronic device cooling, energy storage units, and rotating machinery where surface motion and internal heating coexist. The interaction between buoyancy forces and externally imposed flow introduces a complex coupling in the governing momentum and energy equations, making the analysis more intricate compared to pure forced or free convection scenarios.

In the present study, mixed convection is modeled by introducing a buoyancy term in the momentum equation, which is sensitive to the local temperature difference between the wall and the surrounding fluid. Yuge [1] conducted experiments on heat transfer between spheres and airflow across a wide range of Reynolds (3.5 to 1.44×10^5) and Grashof (1 to 10^5) numbers. Empirical correlations were developed for forced, natural, and mixed convection regimes. A graphical method was proposed to estimate heat transfer performance under combined convection conditions, with comparisons to prior studies. Hieber et al. [2] and Chen et al. [3] investigated the Mixed convection from a sphere at small Reynolds and Grashof numbers. Pop et al. [4] numerically studied steady mixed convection nanofluid flow over a sphere using the Keller-box method, considering both assisting and opposing flows. They found that increasing nanoparticle volume fraction (ϕ) enhances surface heat transfer and skin friction for Al_2O_3, Cu, and TiO_2 in water-based fluids. Eiyad and Chamkha [5] numerically studied

https://doi.org/10.71058/jodac.v9i12004

steady mixed convection in a lid-driven inclined square enclosure filled with water–Al_2O_3 nanofluid using a finite-volume method. Their analysis shows how nanoparticle concentration and inclination angle influence flow behavior and heat transfer performance. The steady hybrid nanofluid flow over a permeable cone and wedge was analyzed by yahaya et al. [6] with thermal radiation and convective effects, revealing that only the first of the triple solutions is stable. Very recently, several studies [7–10] have investigated mixed and natural convection flows, highlighting their complex interaction between buoyancy and inertial forces and their significant impact on thermal and velocity boundary layers.

The demand for high-efficiency thermal systems in industries such as electronics cooling, aerospace, and energy conversion has driven significant research into enhancing heat transfer capabilities. Conventional heat transfer fluids such as water, ethylene glycol, and oil often fall short in meeting the thermal demands of advanced applications. To overcome these limitations, nanofluids; a class of engineered fluids formed by dispersing nanoparticles into a base fluid have emerged as a promising alternative due to their superior thermal conductivity and tunable physical properties. These fluids were conceptualized by Choi [11] and are recognized for their significantly improved thermal performance compared to conventional liquids. The presence of nanoparticles enhances thermal conductivity and convective heat transfer due to their high surface area and superior thermal characteristics (Das et al. [12], Eastman [13]). Such enhanced thermal properties make nanofluids ideal for applications where efficient heat dissipation is essential. They are widely utilized in sectors such as electronics cooling, automotive systems, power generation, medical devices, and advanced energy systems like solar collectors and compact heat exchangers [14-16]. By incorporating nanofluids into these technologies, systems can achieve greater

https://doi.org/10.71058/jodac.v9i12004

energy efficiency, miniaturization, and operational reliability by Xuan and Li [17]. Buongiorno [18], who introduced a comprehensive model for convective transport in nanofluids, accounting for slip mechanisms such as Brownian motion and thermophoresis, thereby laying the theoretical foundation for nanofluid heat transfer analysis. Building on this, Khanafer et al. [19] investigated buoyancy-driven heat transfer in enclosures and demonstrated the significant enhancement in thermal transport when nanofluids are employed. Similarly, Tiwari and Das [20] extended the investigation to a two-sided lid-driven cavity, highlighting how nanoparticle concentration and cavity motion influence heat transfer augmentation. Sampath Kumar et al. [21] explored the combined effects of radiative heat transfer, Joule heating, and Coriolis forces on ferrofluids, emphasizing the complex interplay between magnetic and thermal effects in rotating systems. The relevance of magnetohydrodynamics was further studied by Tshivhi and Makinde [22], who analyzed magneto-nanofluid flows over shrinking/stretching surfaces and revealed dual solutions and their stability characteristics. Moreover, Hayat and Nadeem [23] examined hybrid nanofluids comprising Ag–CuO nanoparticles in water, reporting notable enhancement in heat transfer, thus promoting the potential of hybrid suspensions. In recent developments, Sushma et al. [24] analyzed entropy generation in porous fins wetted with SWCNT and MWCNT-based nanofluids under magnetic effects, providing insights into thermodynamic optimization. Finally, Das and Jana [25] studied natural convection and radiative heat transfer in a magneto-nanofluid environment near a moving vertical plate, reinforcing the importance of radiative and magnetic contributions in free convection flows. Jyoti et al. [26] conducted a detailed analysis of radiative heat transfer and nonlinear convection effects in the flow of kerosene-based alumina nanofluid confined between two parallel plates, accounting for the influence of temperature-dependent

https://doi.org/10.71058/jodac.v9i12004

viscosity. Nasir et al. [27] applied computational intelligence methods to analyze the heat transfer behavior of a Cu + Al_2O_3 + TiO_2/$C_2H_6O_2$ trihybrid nanofluid. The flow was studied over a stretching Riga sheet in a Darcy–Forchheimer porous medium under slip conditions. Effects such as viscous dissipation, radiation, heat sources, and chemical reactions were considered. Esmaeili and Sheikholeslami [28] investigated bio-inspired finned mini-channels for battery cooling, enhancing heat transfer using Fe_3O_4–SWCNT/water hybrid nanofluid. The dolphin- and fish-shaped fins improved thermal performance under laminar flow during high-discharge conditions. Chamkha et al. [29] investigated by Soret–Dufour mass transfer effects on radiative chemically dissipative MHD plain convective water nanofluid (Al2O3, Cu, Ag, & TiO2) flow across a temperature.

By integrating mixed convection effects into the mathematical model, the present work aims to reflect real-world scenarios more accurately, providing valuable insights for the design and optimization of advanced thermal systems employing copper–water nanofluids in electromagnetic environments. Additionally, internal heat generation, particularly when it varies spatially, is an important phenomenon in many thermal systems such as nuclear reactors, electronic substrates, and chemical reactors. Ignoring such effects may lead to inaccurate predictions of temperature fields and inefficient thermal system designs. Several researchers have contributed to understanding the combined effects of convection, and internal heat generation. Turkoglu and Yücel [32] explored mixed convection in vertical channels with discrete heat sources, highlighting localized thermal effects. Mehmood et al. [33] investigated the role of non-uniform heat sources and magnetic fields in doubly stratified magnetonanofluid flow, while Abbasian Arani et al. [34] focused on optimal placement of discrete heat sources in nanofluid-filled cavities to enhance thermal performance.

https://doi.org/10.71058/jodac.v9i12004

Juliyanto et al. [35] analyzed mixed convection over horizontal cylinders with internal heat generation in nanofluids. Zainodin et al. [36] presented an in-depth study on the influence of heat sources on hybrid ferrofluid flow over inclined shrinking surfaces. Haq et al. [37] examined nanofluid flow and heat transfer over inclined irregular surfaces under combined effects of heat sources and chemical reactions. More recently, Vijay Kumar et al. [38] analyzed hybrid nanofluids over a vertical stretching cylinder influenced by radial magnetic fields, with a focus on thermal stratification and heat source/sink dynamics.

Despite extensive work in the field of nanofluid heat transfer, limited studies have focused on the combined effects of magnetic fields, thermal radiation, viscous dissipation, Joule heating, and spatially dependent internal heat generation for copper–water nanofluids in three-dimensional boundary layer flows. Moreover, many previous works simplify the thermal model by neglecting key energy sources or assume steady, low-dimensional scenarios. To bridge this gap, the present study develops a comprehensive three-dimensional boundary layer model for copper–water nanofluid flow over a stretching surface, incorporating the full spectrum of electromagnetic and thermal effects. The governing partial differential equations are formulated under the boundary layer approximations and transformed into a system of nonlinear ordinary differential equations using similarity variables. The numerical solution is obtained using the shooting technique in combination with the Runge-Kutta-Fehlberg method, which ensures accuracy and efficiency.

2. Mathematical Modeling and Physical Configuration

Consider a steady, incompressible, and laminar three-dimensional boundary layer flow of a water-based nanofluid containing copper nanoparticles. The flow is induced by a nonlinearly stretching surface, which extends in both the axial (X) and transverse

https://doi.org/10.71058/jodac.v9i12004

(Y) directions from a common origin. The surface velocities in both directions are prescribed by a power-law form, $U_W = a(X + Y)^n$ and $V_W = b(X + Y)^n$, where a, b and n are positive constants representing the stretching rate along X and Y directions and the nonlinear stretching index, respectively. The nanofluid is electrically conducting and subjected to an externally applied magnetic field that varies spatially. Specifically, a transverse magnetic field of the form $B = B_0(X + Y)^{n-2}$ acts along the Z-axis, where B_0 denotes the magnetic field intensity constant. Due to the assumption of a low magnetic Reynolds number, the induced magnetic field is negligibly small compared to the applied field and is therefore excluded from the analysis.

Thermally, the surface of the sheet is maintained at a constant elevated temperature T_w, while the fluid far from the surface remains at the ambient temperature T_∞ This setup forms the basis for modeling the combined effects of nonlinear stretching, electromagnetic forces, and thermal gradients on the nanofluid flow and heat transfer characteristics. The physical scenario under consideration, as depicted in Fig. 1.

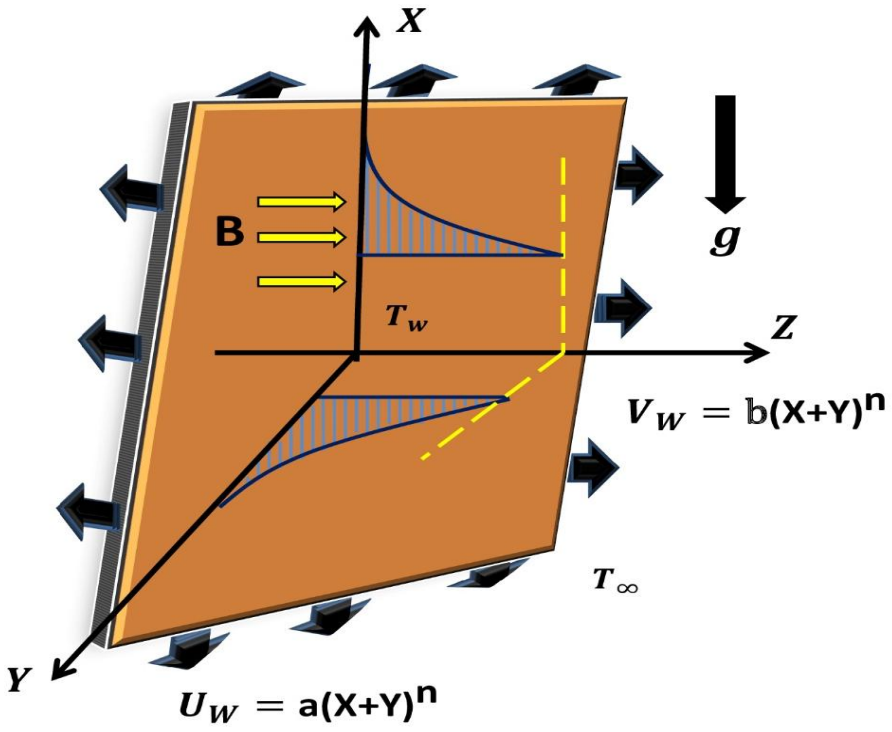

Fig. 1: Geometry of The Problem

https://doi.org/10.71058/jodac.v9i12004

To accurately model the effective properties of the nanofluid, various theoretical and experimental formulations have been proposed, accounting for factors like particle shape, size, and material characteristics. In the present work, the effective thermal conductivity and dynamic viscosity of the nanofluid are determined using the Maxwell-Garnett model [31] and Brinkman model [30], respectively.

According to Brinkman's correlation, the dynamic viscosity μ_{nf} of the nanofluid is:

$$\mu_{nf} = \frac{\mu_f}{(1-\phi)^{2.5}},$$

where ϕ represents the nanoparticle volume fraction. The effective density ρ_{nf} and specific heat capacity $(\rho c_p)_{nf}$ are expressed as [30,25]:

$$\rho_{nf} = (1-\phi)\rho_f + \phi\rho_s,$$

$$(\rho c_p)_{nf} = (1-\phi)(\rho c_p)_f + \phi\left(\rho c_p\right)_s,$$

$$(\rho\beta_T)_{nf} = (1-\phi)(\rho\beta_T)_f + \phi(\rho\beta_T)_s,$$

The Maxwell-Garnett formula is applied to determine the effective thermal conductivity k_{nf} relative to the base fluid conductivity k_f:

$$\frac{k_{nf}}{k_f} = \frac{(k_s+2k_f)-2\phi(k_f-k_s)}{(k_s+2k_f)+\phi(k_f-k_s)},$$

Furthermore, the effective electrical conductivity σ_{nf} is modeled following Maxwell's theory [31] as:

$$\frac{\sigma_{nf}}{\sigma_f} = 1 + \frac{3(\sigma_s-\sigma_f)\phi}{(\sigma_s+2\sigma_f)-(\sigma_s-\sigma_f)\phi},$$

Here, the subscripts s and f refer to the solid nanoparticles and base fluid, respectively.

The governing equations are given as follows;

https://doi.org/10.71058/jodac.v9i12004

$$\frac{\partial U}{\partial X}+\frac{\partial U}{\partial Y}+\frac{\partial W}{\partial Z}=0, \tag{2.1}$$

$$\rho_{nf}\left(U\frac{\partial U}{\partial X}+V\frac{\partial U}{\partial Y}+W\frac{\partial U}{\partial Z}\right)=\mu_{nf}\left(\frac{\partial^2 U}{\partial X^2}+\frac{\partial^2 U}{\partial Y^2}+\frac{\partial^2 U}{\partial Z^2}\right)+\frac{g^*(\rho\beta_T)_{nf}}{\rho_{nf}}(T-T_\infty)-\sigma_{nf}B^2U, \tag{2.2}$$

$$\rho_{nf}\left(U\frac{\partial V}{\partial X}+V\frac{\partial V}{\partial Y}+W\frac{\partial V}{\partial Z}\right)=\mu_{nf}\left(\frac{\partial^2 V}{\partial X^2}+\frac{\partial^2 V}{\partial Y^2}+\frac{\partial^2 V}{\partial Z^2}\right)-\sigma_{nf}B^2V, \tag{2.3}$$

$$\begin{aligned}U\frac{\partial T}{\partial X}+V\frac{\partial T}{\partial Y}+W\frac{\partial T}{\partial Z}=\alpha_{nf}\left(\frac{\partial^2 T}{\partial X^2}+\frac{\partial^2 T}{\partial Y^2}+\frac{\partial^2 T}{\partial Z^2}\right)-\frac{1}{(\rho C_p)_{nf}}\frac{\partial q_r}{\partial Z}+\frac{\mu_{nf}}{(\rho C_p)_{nf}}\left[\left(\frac{\partial U}{\partial Z}\right)^2+\left(\frac{\partial V}{\partial Z}\right)^2\right]\\+\frac{\sigma_{nf}B^2}{(\rho C_p)_{nf}}\left[U^2+V^2\right]+\frac{Q_T}{(\rho C_p)_{nf}}\left(T_f-T_\infty\right)\\+\frac{Q_E}{(\rho C_p)_{nf}}\left(T_f-T_\infty\right)e^{-n\sqrt{\frac{a}{\nu_f}(X+Y)^{\frac{n-1}{2}}Z}}\end{aligned} \tag{2.4}$$

The relevant boundary conditions for the present problem are;

$$U=U_w+\frac{2-\sigma_v}{\sigma_v}\lambda_1\frac{\partial U}{\partial Z},V=V_w+\frac{2-\sigma_v}{\sigma_v}\lambda_1\frac{\partial V}{\partial Z},W=0,T=T_w+K^*\frac{\partial T}{\partial Z}\ at\quad Z=0,$$

$$U\to 0,\quad V\to 0,\quad T\to T_\infty\quad \text{as}\quad Z\to\infty, \tag{2.5}$$

where U, V, and W are usual velocity components in X, Y and Z directions respectively, ρ_{nf} -density of the nanofluid, μ_{nf} -dynamic viscosity of nanofluid, α_{nf} - thermal diffusivity of nanofluid, C_p-specific heat at constant pressure, B_0-applied magnetic field strength, σ_v -tangential momentum accommodation coefficient, λ_1 and K^*- are velocity and thermal slip factor, respectively, and they are assumed to be of variable kinds, where $\lambda_1=\lambda_0(X+Y)^{\frac{1-n}{2}}$ and $K^*=K(X+Y)^{\frac{1-n}{2}}$, where λ_0 and K are constants k_{nf}-thermal conductivity of nanofluid, T -temperature, $q_r=-\left(\frac{4\sigma^*}{3k^*}\right)\frac{\partial T^4}{\partial Z}$ is the Rosseland radiative heat flux, σ^* -Stefan-Boltzman constant and k^* - mean absorption coefficient.

Consider the following three-dimensional nonlinear-type similarity transformations;

$$U=a(X+Y)^n f'(\eta),V=a(X+Y)^n g'(\eta),$$

$$W=-\sqrt{a\nu_f}(X+Y)^{\frac{n-1}{2}}\left(\frac{n+1}{2}\left(f(\eta)+g(\eta)\right)+\frac{n-1}{2}\eta\left(f'(\eta)+g'(\eta)\right)\right),$$

https://doi.org/10.71058/jodac.v9i12004

$$T - T_\infty = (T_w - T_\infty)\theta(\eta), \eta = \sqrt{\frac{a}{\nu_f}}(X+Y)^{\frac{n-1}{2}}Z. \tag{2.6}$$

In view of (2.6), the continuity Eq. (2.1) is identically satisfied, whereas Eqs. (2.2) - (2.5) are follows;

$$\frac{1}{(1-\phi)^{2.5}}f'''(\eta) + \left(1-\phi+\phi\frac{(\rho\beta_T)_s}{(\rho\beta_T)_f}\right)\lambda\theta(\eta) - \left(1+\frac{3\left(\frac{\sigma_s}{\sigma_f}-1\right)\phi}{\frac{\sigma_s}{\sigma_f}+2-\left(\frac{\sigma_s}{\sigma_f}-1\right)\phi}\right)Mf'(\eta)$$

$$+\left(1-\phi+\phi\frac{\rho_s}{\rho_f}\right)\left(\frac{n+1}{2}\big(f(\eta)+g(\eta)\big)f''(\eta) - n\big(f'(\eta)+g'(\eta)\big)f'(\eta)\right) = 0, \tag{2.7}$$

$$\frac{1}{(1-\phi)^{2.5}}g'''(\eta) - \left(1+\frac{3\left(\frac{\sigma_s}{\sigma_f}-1\right)\phi}{\frac{\sigma_s}{\sigma_f}+2-\left(\frac{\sigma_s}{\sigma_f}-1\right)\phi}\right)Mg'(\eta)$$

$$+\left(1-\phi+\phi\frac{\rho_s}{\rho_f}\right)\left(\frac{n+1}{2}\big(f(\eta)+g(\eta)\big)g''(\eta) - n\big(f'(\eta)+g'(\eta)\big)g'(\eta)\right) = 0, \tag{2.8}$$

$$\frac{k_{nf}}{k_f}\frac{1}{pr}(1+R)\theta''(\eta) + \left(1-\phi+\phi\frac{(\rho C_p)_s}{(\rho C_p)_f}\right)\left(\frac{n+1}{2}\big(f(\eta)+g(\eta)\big)\right)\theta'(\eta)$$

$$+\frac{Ec}{(1-\phi)^{2.5}}\left(\big(f''(\eta)\big)^2+\big(g''(\eta)\big)^2\right) + Qt\theta(\eta) + exp(-n\eta)Qe\theta(\eta)$$

$$+MEc\left(1+\frac{3\left(\frac{\sigma_s}{\sigma_f}-1\right)\phi}{\frac{\sigma_s}{\sigma_f}+2-\left(\frac{\sigma_s}{\sigma_f}-1\right)\phi}\right)\left(\big(f'(\eta)\big)^2+\big(g'(\eta)\big)^2\right) = 0. \tag{2.10}$$

Corresponding boundary conditions are,

$$f'(\eta) = 1 + Af''(\eta), g'(\eta) = C + Ag''(\eta), \theta(\eta) = 1 + B\theta'(\eta),$$

$$f(\eta) = 0, g(\eta) = 0 \text{ at } \eta = 0$$

$$f'(\eta) \longrightarrow 0, g'(\eta) \longrightarrow 0, \theta(\eta) \longrightarrow 0 \text{ as } \eta = \infty. \tag{2.11}$$

where $M,\ \lambda, R, Pr, A, B, C, Qt, Qe, n, Ec, Gr_x$ and Re_x^2 are correspondingly magnetic parameter, mixed convection parameter, radiation parameter, Prandtl number, velocity slip parameter, thermal slip parameter, stretching ratio parameter, exponential heat source parameters, exponential index, Eckert number, local Grashof number, local Reynolds number. These governing parameters are defined as;

https://doi.org/10.71058/jodac.v9i12004

$$M = \frac{\sigma_f B_0^2}{a\rho_f}, \lambda = \frac{Gr_x}{Re_x^2}, R = \frac{16\sigma^* T_\infty^3}{3k^* k_f}, A = \frac{2-\sigma_v}{\sigma_v}\lambda_0\sqrt{\frac{a}{\nu_f}},\ B = K\sqrt{\frac{a}{\nu_f}},\ C = \frac{b}{a},$$

$$Qt = \frac{Q_T}{(\rho C_p)_f a}, Qe = \frac{Q_E}{(\rho C_p)_f a}, Ec = \frac{a^2}{(T_w - T_\infty)C_{pf}}, Gr_x = \frac{g\beta_{Tf}(T_w - T_\infty)(X+Y)^3}{\nu_f^3},$$

$$Re_x^2 = \frac{U_w(X+Y)}{\nu_f}.$$

The skin-friction coefficients and local Nusselt number are defined by the following relations;

$$C_{fX} = \frac{\tau_{zx}}{\rho_f U_w^2}, C_{fY} = \frac{\tau_{zy}}{\rho_f V_w^2}, Nu = \frac{(X+Y)q_w}{k_f(T_w - T_\infty)}, \tag{2.12}$$

&

$$\tau_{zX} = \mu_{nf}\left(\frac{\partial U}{\partial Z} + \frac{\partial W}{\partial X}\right)_{Z=0}, \tau_{zY} = \mu_{nf}\left(\frac{\partial V}{\partial Z} + \frac{\partial W}{\partial Y}\right)_{Z=0},$$

$$\mathrm{q_w} = k_{nf}\left(\frac{\partial T}{\partial Z}\right)_{Z=0} + (q_r)_w \tag{2.12}$$

Therefore, Eq. (2.12) will take the following form;

$$\sqrt{Re_X}C_{fX} = \frac{1}{(1-\phi)^{0.5}}f''(0), \sqrt{Re_Y}C_{fY} = \frac{1}{(1-\phi)^{0.5}}f''(0),$$

$$\frac{Nu}{\sqrt{Re_X}} = -\frac{k_{nf}}{k_f}(1+R)\theta'(0).$$

Where $Re_X = \frac{U_w(X+Y)}{\nu_f}$ and $Re_Y = \frac{V_w(X+Y)}{\nu_f}$ are local Reynolds number along X and Y directions respectively.

3. Results and Discussion

This section presents the numerical analysis of three-dimensional slip flow and heat transfer in a copper–water nanofluid over a nonlinear stretching sheet. The governing equations, transformed using similarity variables, are numerically solved via the shooting method. The resulting profiles for primary velocity $f'(\eta)$, secondary velocity $g'(\eta)$, and temperature $\theta(\eta)$ are plotted in each figure, represented consistently by black, red, and blue curves, respectively. In each graph, the influence of a specific parameter is examined while holding the remaining parameters constant, with their

https://doi.org/10.71058/jodac.v9i12004

values clearly specified in the respective figure legends. The line styles solid, dashed, and dotted are used to differentiate between various values of the parameter being varied. Figure 3.2 shows that increasing the mixed convection parameter enhances the x-direction velocity due to stronger buoyancy forces acting in that direction, as reflected in the momentum equation. Conversely, the y-direction velocity decreases. Since buoyancy forces dominate over viscous forces, stronger buoyancy corresponds to lower temperatures, making the x-velocity trend qualitatively opposite to that of the temperature profile. Figure 3.3 illustrates the impact of the magnetic parameter M on the velocity components $f'(\eta)$, $g'(\eta)$, and the temperature profile $\theta(\eta)$. It is evident that as M increases from 0.5 to 1.5, both velocity components decrease. This trend indicates that a stronger magnetic field suppresses the fluid motion due to the Lorentz force, which resists the flow in both x- and y-directions. Conversely, the temperature profile increases with rising M. This behavior is attributed to the fact that the magnetic field induces a resistive force that converts kinetic energy into thermal energy, thereby enhancing the thermal boundary layer thickness. Overall, increasing the magnetic parameter leads to a deceleration in fluid motion and a corresponding rise in temperature due to enhanced Joule heating effects.

Figures 3.4 and 3.5 illustrate the influence of velocity slip parameter A and thermal slip parameter B on $f'(\eta)$, $g'(\eta)$ and $\theta(\eta)$. Increasing A from 0.5 to 2.0 leads to a noticeable decrease in velocity profiles, while increase the surface temperature gradient. This is due to the weakening of the no-slip boundary condition, which reduces shear near the wall, thereby diminishing momentum. The slip condition allows fluid to move more freely along the surface, leading to lower velocity gradients. In Figure 3.5, as B increases from 0.3 to 0.9, the temperature profile significantly increases, while changes in velocity profiles are minimal. The rise in $\theta(\eta)$ is attributed to reduced heat

https://doi.org/10.71058/jodac.v9i12004

conduction from the surface caused by thermal slip, which lowers the surface temperature gradient and thickens the thermal boundary layer. This effect underscores the role of thermal slip in limiting heat transfer efficiency. Overall, both velocity and thermal slip parameters play crucial roles in modulating fluid motion and thermal behavior. Higher slip reduces wall friction and thermal conduction, thereby impacting boundary layer thickness and energy transport characteristics. Figure 3.6 demonstrates that increasing the stretching ratio $C = b/a$ boosts the transverse velocity while reducing the streamwise component. A higher C favors motion in the y-direction, while also intensifying the entrainment of ambient fluid, which strengthens the thermal gradient and results in a thicker thermal boundary layer.

Figure 3.7 illustrates the influence of the Eckert number (Ec) on the temperature profiles. As Ec increases, a significant rise in the temperature profile θ(η) is observed, indicating enhanced thermal energy within the boundary layer. This is attributed to the conversion of kinetic energy into internal energy due to viscous dissipation, which elevates the fluid temperature. Figure 3.8 shows that increasing the power-law index (n) leads to a reduction in both velocity components $f'(\eta), g'(\eta)$ and temperature $\theta(\eta)$. A higher n signifies a shear-thickening (dilatant) fluid, which increases resistance to flow, thereby weakening the velocity fields and thinning the momentum boundary layer. Additionally, reduced fluid motion limits convective heat transfer, resulting in a lower temperature profile.

Figure 3.9 reveals that increasing the nanoparticle volume fraction leads to a reduction in velocity components while significantly enhancing the temperature distribution. This is because higher nanoparticle concentration improves the thermal conductivity of the fluid, resulting in a thicker thermal boundary layer and elevated temperature profiles. The figures 3.10 and 3.11 are evident that increasing exponential

https://doi.org/10.71058/jodac.v9i12004

heat source parameter (Qe and Qt) values of significantly enhance the temperature distribution within the boundary layer. This behavior is due to the intensified internal heat generation, which raises the thermal energy of the fluid. Consequently, higher Qe and Qt lead to a thicker thermal boundary layer, indicating an increase in heat transfer rate. The influence of the thermal radiation parameter R on the velocity and temperature profiles is depicted in the figure 3.12. It is observed that an increase in R significantly elevates the temperature distribution $\theta(\eta)$ across the boundary layer. This is because higher R implies stronger radiative heat transfer, supplying additional energy to the fluid. Consequently, the thermal boundary layer becomes thicker.

Table 3.1 presents the thermo-physical properties of water and copper (Cu) nanoparticles used in the present study. These standard values are adopted from the literature to compute the effective nanofluid properties. Table 3.2 presents the numerical results for the skin friction coefficients and the Nusselt number, highlighting the influence of A, B, C, Ec, and ϕ, both in the absence ($\lambda = 0$) and presence ($\lambda = 2$) of mixed convection. An increase in ϕ intensifies both components of skin friction due to enhanced effective viscosity. Heat transfer is enhanced with higher ϕ when λ=0, but in the presence of mixed convection, the Nusselt number drops and may become negative, indicating a reversal in heat flow direction due to stronger buoyancy effects. The presence of velocity slip reduces the momentum transfer at the wall. When A increases from 0 to 1, $Re_X^{0.5}C_{fX}$ significantly decreases in magnitude (e.g., from –3.3007 to –1.0023 for ϕ=0.2), implying reduced shear stress due to slip weakening the velocity gradient at the surface. A similar decreasing trend is observed in the secondary skin friction component $Re_X^{0.5}C_{fY}$. Thermal slip acts as a resistance to heat transfer at the boundary. For example, increasing B from 0.4 to 1.5 (keeping other parameters constant) causes a reduction in $Re_X^{-0.5}NU$ under mixed convection from –0.6246 to –

https://doi.org/10.71058/jodac.v9i12004

0.4409 indicating a drop in wall heat flux due to thermal insulation effects from the slip condition. Without mixed convection, however, the Nusselt number increases with higher B, showing complex interplay between thermal boundary conditions and forced convection. Higher Ec values amplify the role of viscous dissipation. At $\phi = 0.2$, the Nusselt number increases from 8.6931 to 9.9258 when Ec rises from 0.01 to 0.2 in the absence of mixed convection, demonstrating enhanced thermal energy generation. In contrast, when $\lambda = 2$, the Nusselt number becomes increasingly negative with higher Ec, for instance reaching –1.0107 at $Ec = 2$, suggesting that dissipation-induced heating can counteract convective cooling under buoyancy-dominated flows. Incorporating mixed convection ($\lambda = 2$) leads to significant changes in the thermal and momentum behavior. In most cases, it reduces both skin friction coefficients and the Nusselt number. Notably, the Nusselt number becomes negative in several configurations, indicating reversed heat transfer due to strong opposing buoyancy forces.

Table 3.1: Thermo-physical properties of Water and Copper (Cu) nanoparticles [22, 23, 29].

	Water	$\boldsymbol{Cu}$
$\boldsymbol{C_p}$ $\boldsymbol{[J/kgK]}$	4179	385
$\boldsymbol{\rho}$ $\boldsymbol{[kg/m^3]}$	997.1	8933
$\boldsymbol{k}$ $\boldsymbol{[W/mk]}$	0.613	401
$\boldsymbol{\mu}$ $\boldsymbol{[Ns/m^2]}$	-	-
$\boldsymbol{\beta} \times 10^5$ $\boldsymbol{[1/K]}$	21	1.67
$\boldsymbol{\sigma}$ $\boldsymbol{[Sm^{-1}]}$	0.05	5.96×10^7
$\boldsymbol{Pr}$	23.0114	-

https://doi.org/10.71058/jodac.v9i12004

Table 3.2: Variation of $Re_x^{0.5}C_{fx}$, $Re_x^{0.5}C_{fy}$ and $Re_x^{-0.5}Nu$ under the influence and absence of mixed convection (λ) with for various values of ϕ, A, B, C and Ec.

ϕ	A	B	C	Ec	Absence of mixed convection ($\lambda = 0$)			Presence of mixed convection ($\lambda = 2$)		
					$Re_X^{0.5}C_{fX}$	$Re_X^{0.5}C_{fY}$	$Re_X^{-0.5}NU$	$Re_X^{0.5}C_{fY}$	$Re_X^{0.5}C_{fX}$	$Re_X^{-0.5}NU$
0.2	0.5	0.4	0.6	0.2	-1.598730	-0.959238	9.925833	-1.154884	-1.016947	-0.624587
0.01					-0.879611	-0.527767	-0.436751	-0.562060	-0.560139	0.545656
0.1					-1.175989	-0.705594	-3.088545	-0.805918	-0.749559	-0.089042
0.2					-1.598730	-0.959238	9.925833	-1.154884	-1.016947	-0.624587
	0				-3.300735	-1.980441	0.158452	-2.403520	-2.034680	0.592810
	0.5				-1.598730	-0.959238	9.925833	-1.154884	-1.016947	-0.624587
	1				-1.002315	-0.601389	-5.306444	-0.579952	-0.644109	0.333300
		0.4			-1.598730	-0.959238	9.925833	-1.154884	-1.016947	-0.624587
		0.8			-1.598730	-0.959238	4.282063	-1.134312	-1.019075	-0.544037
		1.5			-1.598730	-0.959238	2.146356	-1.109619	-1.021595	-0.440919
			0.6		-1.598730	-0.959238	9.925833	-1.154884	-1.016947	-0.624587
			1		-1.666573	-1.666573	-4.519695	-1.252881	-1.741215	-0.524239
			2		-1.793039	-3.586077	-1.920984	-1.403071	-3.684522	-1.010966
				0.01	-1.598730	-0.959238	8.693107	-1.212291	-1.010020	0.093328
				0.1	-1.598730	-0.959238	9.277030	-1.184967	-1.013346	-0.246828
				0.2	-1.598730	-0.959238	9.925833	-1.154884	-1.016947	-0.624587

Table 3.3: Variation of $Re_x^{0.5}C_{fx}$, $Re_x^{0.5}C_{fy}$ and $Re_x^{-0.5}Nu$ under the influence and absence of mixed convection (λ) with for various values of M, Qe, Qt, R and n.

https://doi.org/10.71058/jodac.v9i12004

M	Qe	Qt	R	n	Absence of mixed convection ($\lambda = 0$)			Presence of mixed convection ($\lambda = 2$)		
					$Re_X^{0.5}C_{fX}$	$Re_X^{0.5}C_{fY}$	$Re_X^{-0.5}NU$	$Re_X^{0.5}C_{fY}$	$Re_X^{0.5}C_{fX}$	$Re_X^{-0.5}NU$
0.5	0.5	0.5	0.5	2	-1.598730	-0.959238	9.925833	-1.154884	-1.016947	-0.624587
0.5					-1.598730	-0.959238	9.925833	-1.154884	-1.016947	-0.624587
0.8					-1.636127	-0.981676	3.263974	-1.179277	-1.036266	-0.919712
1					-1.659640	-0.995784	2.057032	-1.194747	-1.048447	-1.117144
	0.1				-1.598730	-0.959238	59.561509	-1.210614	-1.010445	0.125913
	0.5				-1.598730	-0.959238	9.925833	-1.154884	-1.016947	-0.624587
	1				-1.598730	-0.959238	5.996665	-1.065313	-1.026898	-1.893573
		0.1			-1.598730	-0.959238	0.533623	-1.294919	-0.998669	0.861245
		0.3			-1.598730	-0.959238	-0.735713	-1.238546	-1.006234	0.270669
		0.5			-1.598730	-0.959238	9.925833	-1.154884	-1.016947	-0.624587
			0.5		-1.598730	-0.959238	9.925833	-1.154884	-1.016947	-0.624587
			2		-1.598730	-0.959238	18.510508	-1.099707	-1.027112	-0.788968
			4		-1.598730	-0.959238	-13.631822	-1.078521	-1.031334	-0.720288
				2	-1.598730	-0.959238	9.925833	-1.154884	-1.016947	-0.624587
				4	-1.797814	-1.078688	-0.233249	-1.556265	-1.116261	0.671514
				8	-2.008604	-1.205162	1.318340	-1.875328	-1.228765	1.572025

https://doi.org/10.71058/jodac.v9i12004

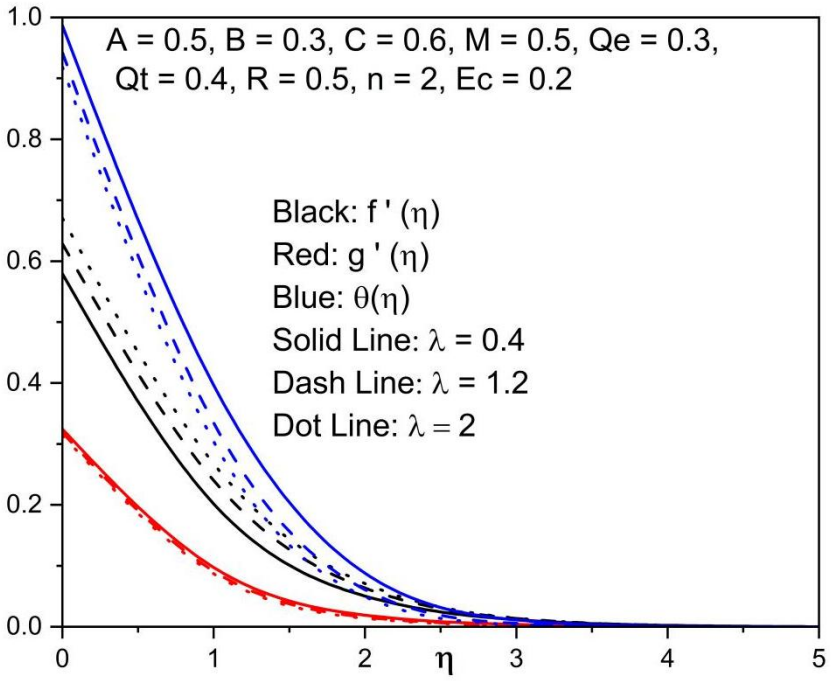

Fig. 3.2: Impact of λ on $f'(\eta), g'(\eta)$ and $\theta(\eta)$.

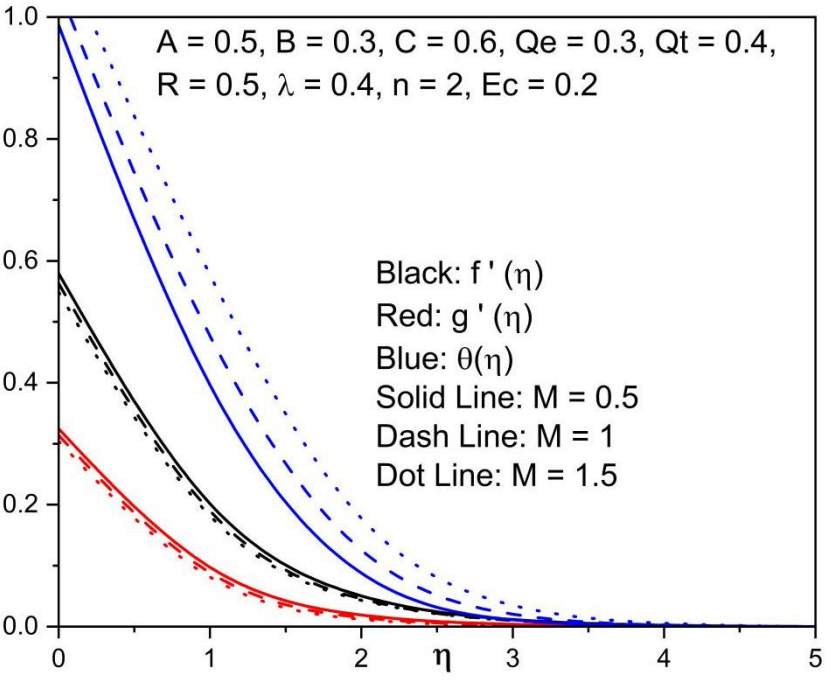

Fig. 3.3: Impact of M on $f'(\eta), g'(\eta)$ and $\theta(\eta)$.

https://doi.org/10.71058/jodac.v9i12004

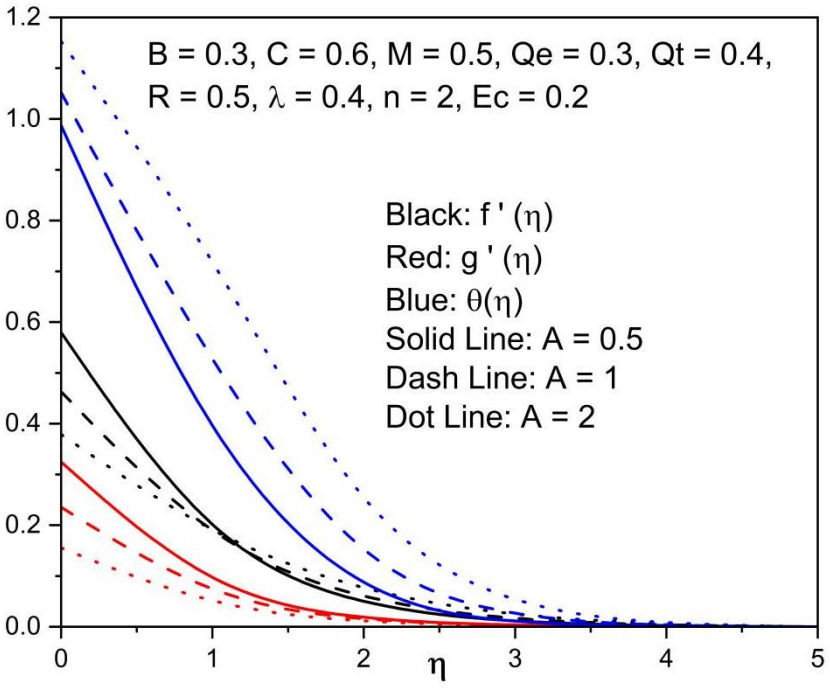

Fig. 3.4: Impact of A on $f'(\eta), g'(\eta)$ and $\theta(\eta)$.

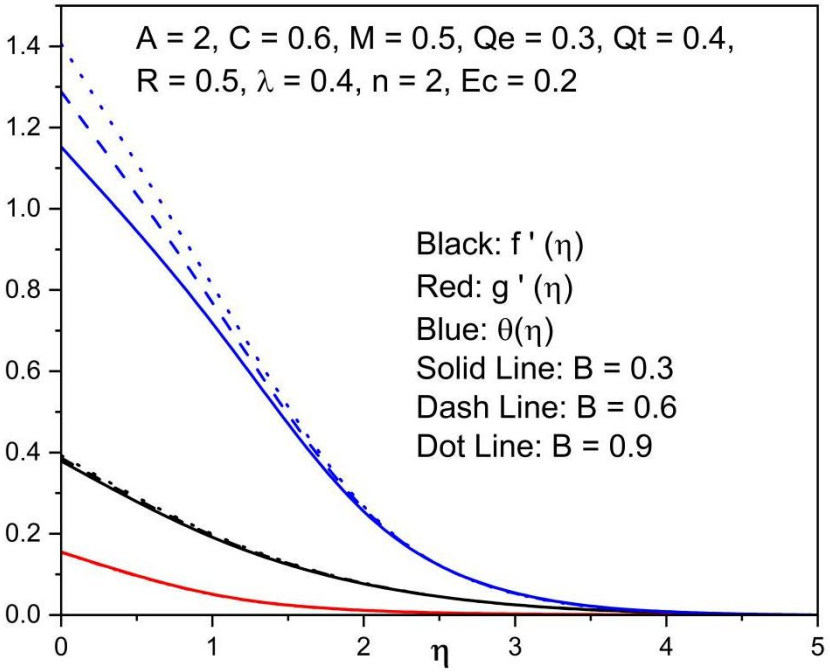

Fig. 3.5: Impact of B on $f'(\eta), g'(\eta)$ and $\theta(\eta)$.

https://doi.org/10.71058/jodac.v9i12004

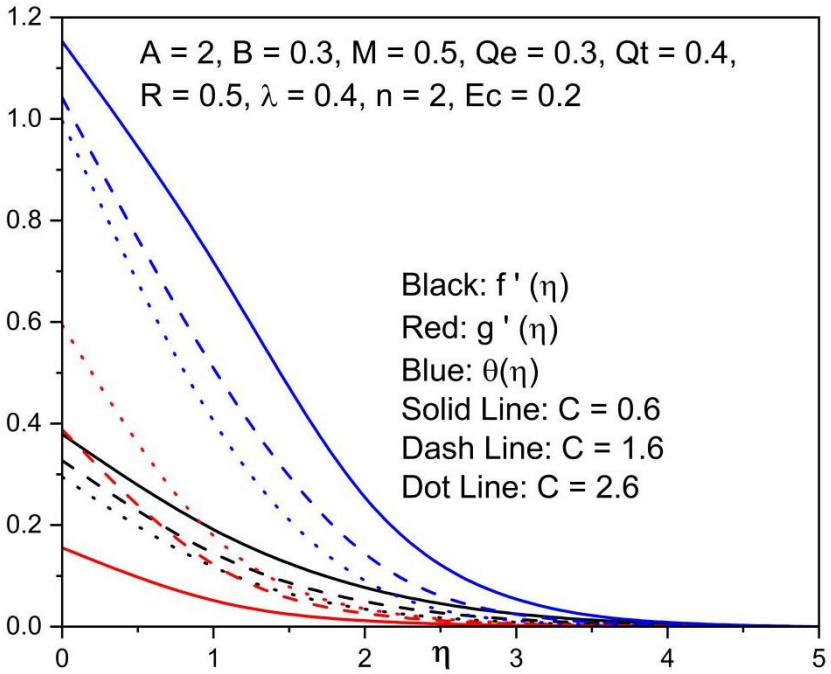

Fig. 3.6: Impact of C on $f'(\eta), g'(\eta)$ and $\theta(\eta)$.

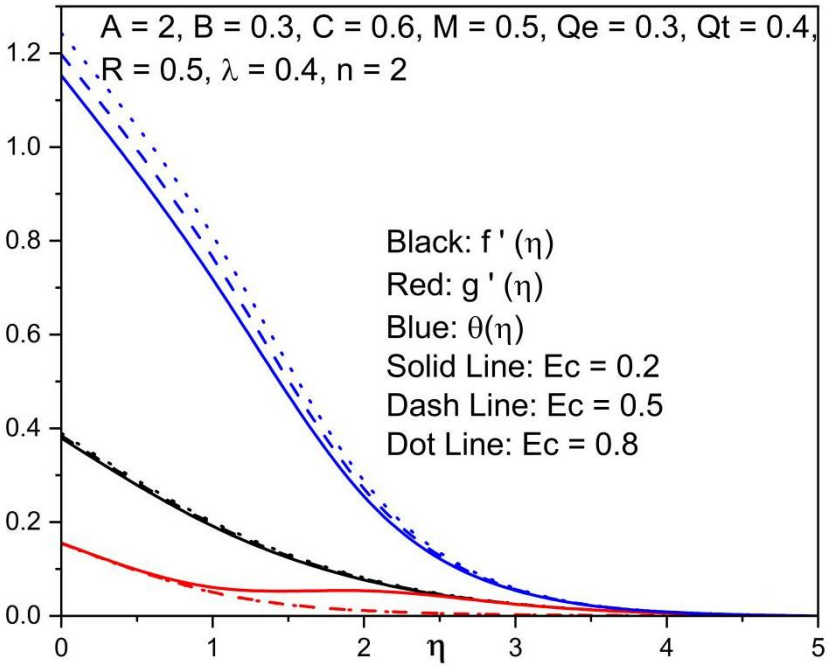

Fig. 3.7: Impact of Ec on $f'(\eta), g'(\eta)$ and $\theta(\eta)$.

https://doi.org/10.71058/jodac.v9i12004

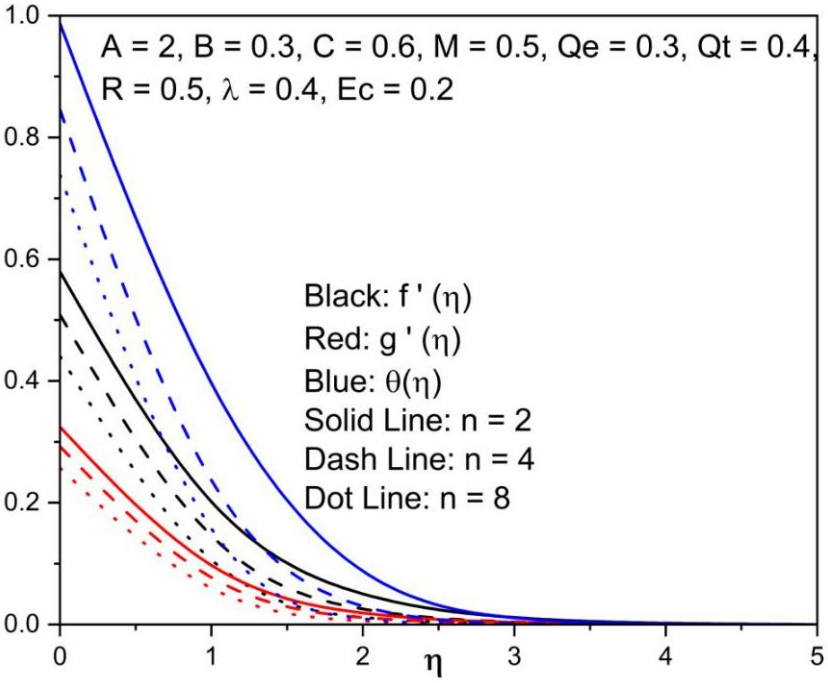

Fig. 3.8: Impact of n on $f'(\eta), g'(\eta)$ and $\theta(\eta)$.

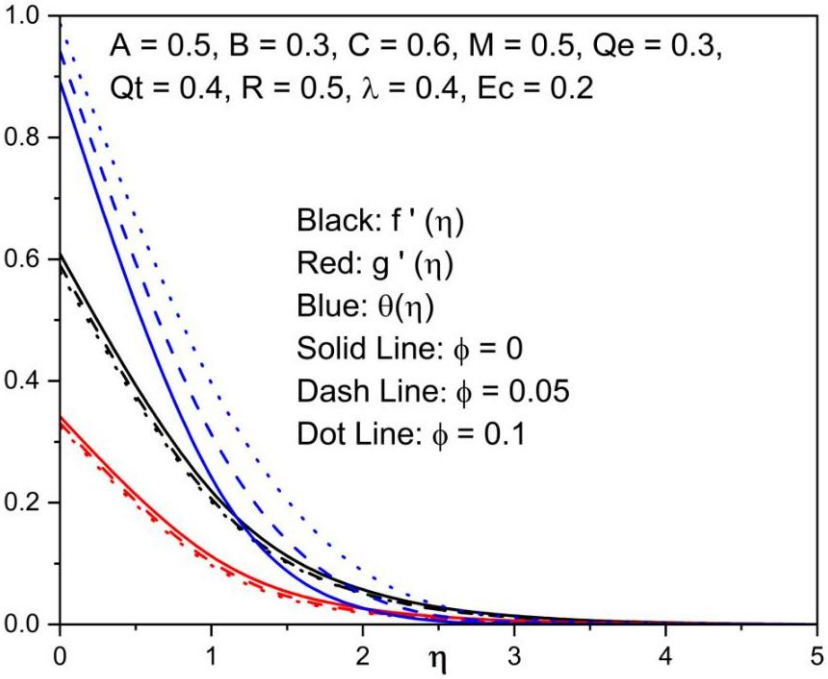

Fig. 3.9: Impact of ϕ on $f'(\eta), g'(\eta)$ and $\theta(\eta)$.

https://doi.org/10.71058/jodac.v9i12004

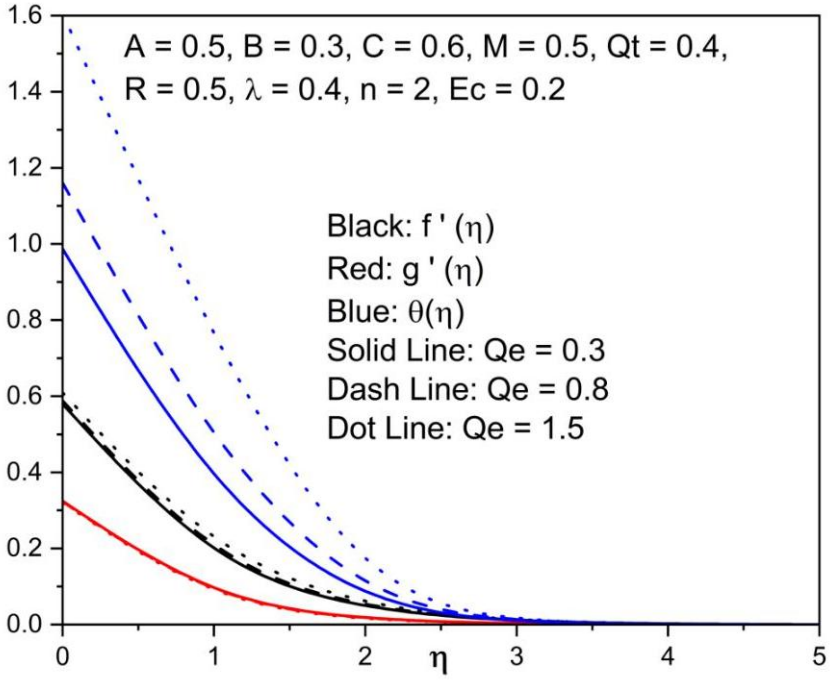

Fig. 3.10: Impact of Qe on $f'(\eta), g'(\eta)$ and $\theta(\eta)$.

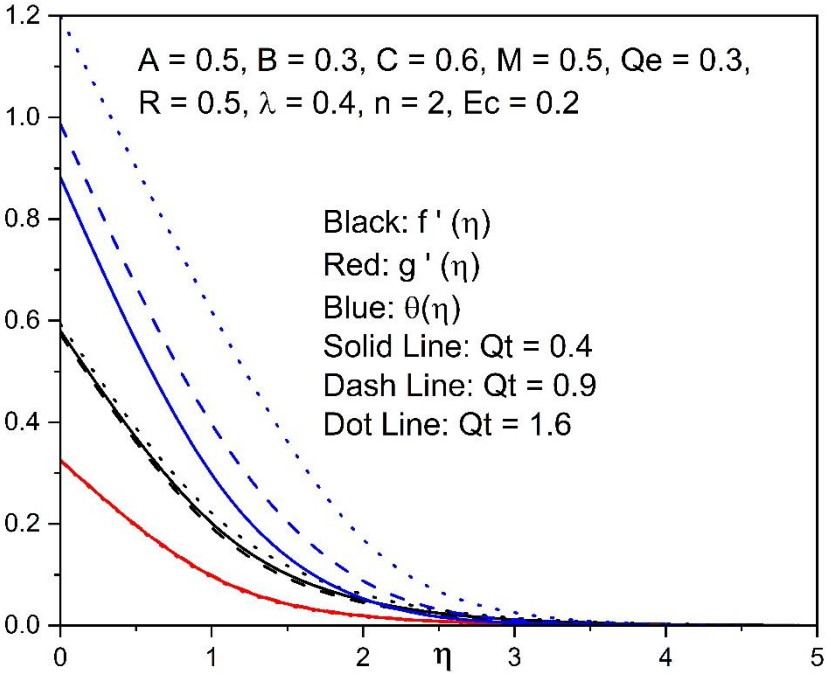

Fig. 3.11: Impact of Qt on $f'(\eta), g'(\eta)$ and $\theta(\eta)$.

https://doi.org/10.71058/jodac.v9i12004

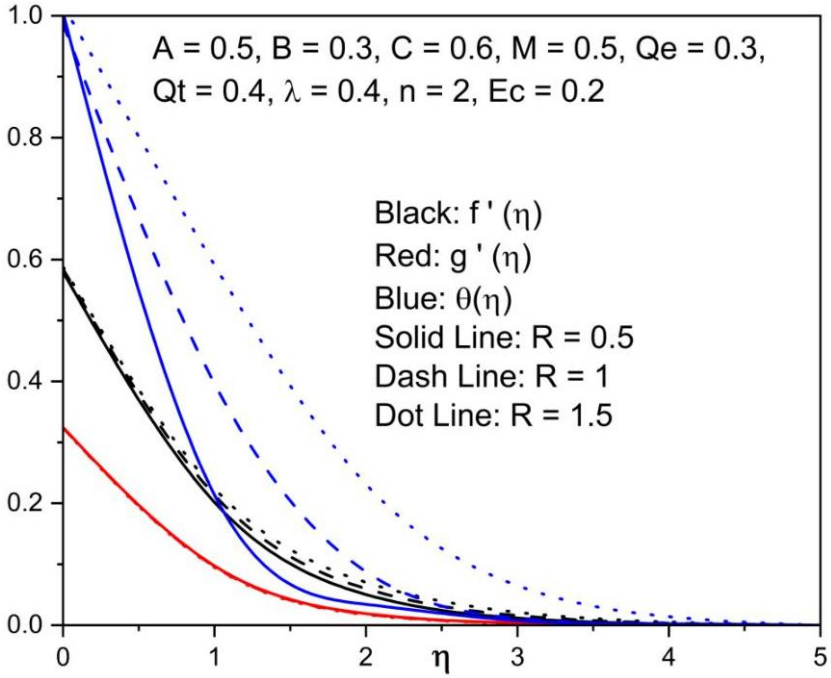

Fig. 3.12: Impact of R on $f'(\eta), g'(\eta)$ and $\theta(\eta)$.

4. Conclusion

This study presents a comprehensive numerical investigation into the three-dimensional slip flow and heat transfer characteristics of copper–water nanofluids over a nonlinearly stretching surface under the combined influence of magnetic field, thermal radiation, viscous dissipation, Joule heating, and exponentially varying internal heat sources. Some Significant Points of the Problem Are Summarized Below:

- Enhanced buoyancy (λ) improves the streamwise velocity but reduces temperature due to stronger convective cooling.
- The magnetic field suppresses fluid motion while raising temperature via Joule heating.
- The temperature profile is elevated with increasing values of the slip parameters A (velocity slip) and B (thermal slip)
- Exponential heat generation further elevates fluid temperature, particularly near the surface.

https://doi.org/10.71058/jodac.v9i12004

- Copper nanoparticles significantly enhance thermal conductivity, thereby improving heat transfer performance, particularly at higher values of the radiation parameter (R) and Eckert number (Ec).
- The skin friction coefficient in the x-direction is significantly higher under the influence of mixed convection than in its absence
- An increase in ϕ intensifies both components of skin friction due to enhanced effective viscosity. Heat transfer is enhanced with higher ϕ when $\lambda=0$, but in the presence of mixed convection, the Nusselt number drops and may become negative, indicating a reversal in heat flow direction due to stronger buoyancy effects.

5. Declarations

5.1 Competing interests:

The author affirms that there is no conflict of interest related to the publishing of this work

5.2 Funding:

This research did not receive any specific grant from funding agencies in the public, commercial, or not-for-profit sectors.

5.3 Acknowledgments:

We are grateful to the reviewers and editors for their constructive suggestions

5.4 Data availability:

The data supporting this study's findings are available within the article.

https://doi.org/10.71058/jodac.v9i12004

References

1. Yuge T. Experiments on heat transfer from spheres including combined natural and forced convection. Journal of Heat Transfer. 1960; 82(3):214-220.
2. Hieber CA, Gebhart B. Mixed convection from a sphere at small Reynolds and Grashof numbers. Journal of Fluid Mechanics. 1969; 38(1): 137-159.
3. Chen TS, Aleksandros M. Analysis of mixed forced and free convection about a sphere. International Journal of Heat and Mass Transfer. 1977; 20(8): 867-875.
4. Tham L., Nazar R, Pop I. Mixed convection boundary-layer flow about an isothermal solid sphere in a nanofluid. Physica Scripta. 2011; 84(2): 025403.
5. Abu-Nada, Eiyad, Chamkha Ali J. Mixed convection flow in a lid-driven inclined square enclosure filled with a nanofluid. European Journal of Mechanics-B/Fluids. 2010; 29(6): 472-482.
6. Yahaya RI, Norihan MA, Mustafa MS, Pop I, Ali FM, Siti Suzilliana Putri Mohamed Isa. Mixed convection hybrid nanofluid flow past a non-isothermal cone and wedge with radiation and convective boundary condition: Heat transfer optimization. Case Studies in Thermal Engineering. 2025;66: 105768.
7. Hayat T, Abbas Z, Pop I, Asghar S. Effects of radiation and magnetic field on the mixed convection stagnation-point flow over a vertical stretching sheet in a porous medium. International Journal of Heat and Mass Transfer. 2010;53(1 -3): 466-474.
8. Das S, Jana RN, Natural convective magneto-nanofluid flow and radiative heat transfer past a moving vertical plate. Alex Eng J. 2015;54:55–64
9. Kumar AV, Chamkha, AJ, Doley S, Jino L, Jacob A, Manoj E, Suthan SA, Jayaganthan A. Thermal management of battery cell module using a hybrid nanofluid filled inverted right-angled porous triangular cavity through natural

https://doi.org/10.71058/jodac.v9i12004

convection. *Journal of Thermal Analysis and Calorimetry*. 2024;*149*(17):.9639-9661.

10. Dinarvand S, Pop I, Gangadhar K, Roy NC, Abbasi A, Noeiaghdam S. Unsteady Mixed Convection of Opposing Flow: Dual Solution Report of Two-Particle Nanofluid Behavior Around a Vertical Cylinder. *Journal of Nanofluids*, 2024;*13*(6):1271-1278.
11. Choi, SUS. Enhancing thermal conductivity of fluids with nanoparticles. *ASME FED*. 1995; 231: 99–105.
12. Das SK, Choi SUS, Yu W, Pradeep T. *Nanofluids: Science and Technology*. Wiley-Interscience, 2007.
13. Eastman JA. Thermal transport in nanofluids. *Annual Review of Materials Research*. 2004.
14. Saidur R, Leong KY, Mohammad HA. A review on applications and challenges of nanofluids. *Renewable and Sustainable Energy Reviews*. 2011; 15:1646–1668.
15. Wang X, Xu X, Choi SUS. Thermal conductivity of nanoparticle-fluid mixture. *Journal of Thermophysics and Heat Transfer*. 1999; 13(4):474–480.
16. Murshed SMS, Leong KC, Yang C. Enhanced thermal conductivity of TiO_2-Water based nanofluids. *International Journal of Thermal Sciences*. 2005; 44: 367–373.
17. Xuan Y, Li Q. Heat transfer enhancement of nanofluids. *International Journal of Heat and Fluid Flow*. 2000; 21:58–64.
18. Buongiorno J. Convective transport in nanofluids. *Journal of Heat Transfer*. 2006; 128:240–250.
19. Khanafer K, Vafai K, Lightstone M. Buoyancy-driven heat transfer enhancement in a two-dimensional enclosure utilizing nanofluids. *International Journal of Heat and Mass Transfer.* 2003; 46: 3639–3653.

https://doi.org/10.71058/jodac.v9i12004

20. Tiwari RK, Das MK. Heat transfer augmentation in a two-sided lid-driven differentially heated square cavity utilizing nanofluids. *International Journal of Heat and Mass Transfer*. 2007; 50:2002–2018.
21. Sampath Kumar PB, Gireesha BJ, Mahanthesh **B**, Gorla RSR. Radiative nonlinear 3D flow of ferrofluid with Joule heating, convective condition and Coriolis force. Thermal Science and Engineering Progress. 2017; 3:88-94.
22. Tshivhi KS, Makinde OD. Magneto-nanofluid coolants past heated shrinking/stretching surfaces: dual solutions and stability analysis. *Results in Engineering*. 2021; *10*:100229.
23. Hayat T, Nadeem S. Heat transfer enhancement with Ag–CuO/water hybrid nanofluid. *Results in physics*. 2017:*7*:2317-2324.
24. Sushma S, Usha B, Gireesha BJ. Impact of magnetic field on entropy production in porous radial fin wetted by water and engine oil-based SWCNTs and MWCNTs. *International Journal of Ambient Energy*. 2025; *46*(1):2483536.
25. Das S, Jana RN. Natural convective magneto-nanofluid flow and radiative heat transfer past a moving vertical plate. Alex Eng J. 2015; 54:55–64.
26. Jyoti DK, Nagaradhika V, Sampath Kumar PB, Chamkha AJ. Nonlinear Convection and Radiative Heat Transfer in Kerosene-Alumina Nanofluid Flow Between Two Parallel Plates with Variable Viscosity. Journal of Nanofluids. 2024; 13(5): 1055-1062.
27. Nasir S, Berrouk AS, Gul T. Analysis of chemical reactive nanofluid flow on stretching surface using numerical soft computing approach for thermal enhancement. *Engineering Applications of Computational Fluid Mechanics*. 2024; *18*(1):2340609.

https://doi.org/10.71058/jodac.v9i12004

28. Esmaeili Z, Sheikholeslami M. Enhanced thermal management of lithium-ion batteries using hybrid nanofluids in finned mini-channels: Energy and entropy analyses. *Engineering Science and Technology, an International Journal*. 2025; *66*:102069.
29. Ragulkumar E., Elumalai, P. Sambath KS, Balasubramanian S, Chamkha AJ. Soret–Dufour mass transfer effects on radiative chemically dissipative MHD plain convective water nanofluid (Al2O3, Cu, Ag, & TiO2) flow across a temperature-controlled upright cone surface with heat blow/suction. *Numerical Heat Transfer, Part A: Applications.* 2025; 86(2): 278-296.
30. Brinkman HC, The viscosity of concentrated suspensions and solutions. J. Chem Phys. 1952; 20:571–581.
31. Maxwell JC, A treatise on electricity and magnetism, Second Ed., Cambridge Oxford University Press. 1904; 435-441.
32. Turkoglu H, Yücel N. Mixed convection in vertical channels with a discrete heat source. *Heat and Mass Transfer.* 1995; 30(3): 159-166.
33. Mehmood K, Hussain S, Sagheer M. Mixed convection flow with non-uniform heat source/sink in a doubly stratified magnetonanofluid. *AIP Advances.* 2016; 6(6).
34. Abbasian Arani AA, Abbaszadeh M, Ardeshiri AJTPNMS. Mixed convection fluid flow and heat transfer and optimal distribution of discrete heat source's location in a cavity filled with nanofluid. *Challenges in Nano and Micro Scale Science and Technology.* 2016; 5(1): 30-43.
35. Juliyanto B, Widodo B, Imron C. The effect of heat generation on mixed convection flow in nano fluids over a horizontal circular cylinder. In *Journal of Physics: Conference Series*, 2018; 1008(1): 012001. IOP Publishing.

https://doi.org/10.71058/jodac.v9i12004

36. Zainodin S, Jamaludin A, Nazar R, Pop I. Impact of heat source on mixed convection hybrid ferrofluid flow across a shrinking inclined plate subject to convective boundary conditions. *Alexandria Engineering Journal*. 2024; *87*:662-681.
37. Haq I, Bilal M, Ahammad NA, Mohamed E. Ghoneim AA, Weera W. Mixed convection nanofluid flow with heat source and chemical reaction over an inclined irregular surface. *ACS omega.* 2022; 7(34): 30477-30485.
38. S. Vijay Kumar A. Jakhar P, sharma AK, Anurag. Numerical exploration of heat source/sink and mixed convection effects on thermally stratified Cu− Al 2 O 3/H 2 O \rmCu-\rmAl_2\rmO_3/\rmH_2\rmO hybrid nanofluid flow over a vertical stretching cylinder subjected to a radial magnetic field. *ZAMM-Journal of Applied Mathematics and Mechanics/Zeitschrift für Angewandte Mathematik und Mechanik.* 2025; 105(1): e202400963.